Korean J. Chem. Eng., 37(4), 652-662 (2020)
DOI: 10.1007/s11814-019-0464-y

pISSN: 0256-1115
eISSN: 1975-7220

Adsorption behavior of Ag(I) onto elemental sulfur-encapsulated silica nanocapsules for industrial applications

Norasikin Saman*, Gamal Abdulaziz Mohammed Alaghbari*, Safia Syazana Mohtar*, Helen Kong, Khairiraihanna Johari***, Noorhalieza Ali*, and Hanapi Mat*,****,†**

*Advanced Materials and Process Engineering Laboratory, School of Chemical and Energy Engineering, Faculty of Engineering, Universiti Teknologi Malaysia, 81310 UTM Skudai, Johor, Malaysia
**Centre of Lipid Engineering and Applied Research, School of Chemical and Energy Engineering, Faculty of Engineering, Universiti Teknologi Malaysia, 81310 UTM Skudai, Johor, Malaysia
***Department of Chemical Engineering, Faculty of Engineering, Universiti Teknologi PETRONAS, 32610, Bandar Seri Iskandar, Perak, Malaysia
****Advanced Materials and Separation Technologies (AMSET) Research Group, Health and Wellness Research Alliance, Universiti Teknologi Malaysia, 81310 UTM Skudai, Johor, Malaysia
(*Received 26 August 2019 • accepted 16 December 2019*)

Abstract−Pure silica nanocapsules (SiNC-P) and elemental sulfur-encapsulated silica nanocapsules (SiNC-ES) as Ag(I) adsorbents were successfully synthesized by a one-step water-in-oil microemulsion polymerization process. The characterization of the synthesized materials, such as surface morphology, surface area, porosity, functional groups and thermal characteristics, was carried out using various analytical techniques. The SiNC-P and SiNC-ES have nearly similar morphology, but the surface area and pore size of the SiNC-ES are higher than SiNC-P. The Ag(I) adsorption study showed that it increased with increasing elemental sulfur (ES) amount in the SiNC-ES. The SiNC-ES shows high adsorption capacity, independent of pH, and higher adsorption rate as compared to SiNC-P. The maximum Ag(I) adsorption capacity of SiNC-P and SiNC-ES was 50.49 mg g^{-1} and 98.51 mg g^{-1}, respectively. The adsorption isotherm data were best described by the Langmuir model. The diffusion modeling analysis of the kinetic data indicated that film diffusion is the controlling step, while chemical reaction modeling obeys the pseudo-second-order kinetic model. The SiNC-ES was reusable and good adsorption performance up to four adsorption cycles was observed. The practical capability of the SiNC-ES to adsorb Ag(I) was successfully demonstrated using an industrial waste solution in which a high removal efficiency was observed (η>90%). This demonstrates that the SiNC-ES can be a potential adsorbent for Ag(I) recovery from industrial wastes.

Keywords: Silica, Elemental Sulfur, Nanocapsules, Ag(I) Ions, Adsorption

INTRODUCTION

Silver contamination has increased due to increasing demand for electric and electronic product, photographic, coinage, and metal alloy industries [1,2]. Consequently, the availability of silver from natural sources is also continuously decreasing accordingly. Silver recovery and reutilization from waste water/solid as secondary silver sources has therefore gained considerable attention. An adsorption process is relatively effective and efficient for metal recovery compared to other processes due to their operational complexity, high operational cost and incomplete removal, and toxic wastes [3]. Materials such as activated carbons/chars [4-7], resins [8-15], biomaterials [16-18], clays and zeolites [3,19-21], metal oxides [22], and silicas [1,23-25] have been explored for Ag(I) adsorption in aqueous solution.

With the rapid development of nanotechnology, silica nanocapsules (SiNC) have attracted significant interest as a superior nanocarrier for loading and delivering functional compounds. Various functional compounds have been encapsulated into the silica nanocapsules and used in many potential applications such as drugs and gene delivery vehicles [26-29], imaging agents for imaging probes [27,30-32], catalysts [33,34], sensing coatings [35-38], energy storages [39], and environmental remedies [2,40-43].

As adsorbents, in order to improve the affinity of the SiNC towards selected metal ions, specific modifications by introducing the function groups into SiNC are inevitable. It is well known that the sulfur functional groups have a soft Lewis base property that offers a strong affinity towards soft Lewis acid metals such as Hg(II), Ag(I), and Au(III)) [44,45]. The modification of silica materials using ES has been hardly reported. Most of modifications using ES were performed using a dry impregnation method where the mixture of ES and support materials (e.g., silicas, activated carbons, and synthetic polymers) was heated in a controlled environment [44-46]. The elemental sulfur (ES) encapsulated SiNC (SiNC-ES) synthesized via one-step oil-in-water microemulsion polymerization process in which the hydrophobic phase containing ES molecules was first homogeneously emulsified in water soluble micelle template, followed by the formation of silica wall around the micelles being

†To whom correspondence should be addressed.
E-mail: hbmat@cheme.utm.my

introduced [2,38]. Our previous study shows that the SiNC-ES synthesized using this method offers a good potential to be an adsorbent for treating Hg(II) in aqueous solution [2]. So far, to the best of our knowledge, the application of SiNC-ES as an adsorbent for Ag(I) has not been reported.

Thus, this study was carried out to synthesize and characterize of the pure SiNC (SiNC-P) and elemental sulfur-encapsulated SiNC (SiNC-ES), and finally to investigate the adsorption characteristics of the SiNC-ES towards Ag(I) in aqueous solution at various conditions such as pH, Ag(I) concentration and contact time as compared for some cases to the SiNC-P. The selectivity and regenerability of the SiNC-ES was also studied to demonstrate its industrial potential application for Ag(I) recovery. A selectivity study was carried out using liquid photographic waste.

EXPERIMENTAL

1. Chemicals

The chemicals used in the present study, namely toluene (99%), elemental sulfur (ES) (99%), cetyltrimethylammonium bromide (CTAB, 99%) and tetraethylorthosilicate (TEOS, 99%), ammonium solution (NH_4OH, 25-28%) and silver nitrate salt ($AgNO_3$, 99%), were purchased from Merck (Germany). All chemicals were of analytical reagent grade and used without further purification. All aqueous solutions were prepared using freshly prepared double-distilled water.

2. Preparation of Silica Nanocapsules (SiNC)

Pure silica nanocapsules (SiNC-P) were prepared via microemulsion oil-in-water process, according to the modified procedure reported by Maia et al. [38]. First, aqueous CTAB solution was prepared by dissolving 0.25 g of CTAB in 35 mL of distilled water, and subsequently 0.25 mL of NH_4OH catalyst was added into the solution. 10 mL of toluene (oil phase) was then added into the water phase and the mixture was stirred vigorously until a microemulsion was obtained, followed by dropwise addition of 2.0 mL of TEOS. The flask was kept closed and the mixture was continuously stirred at room condition for 24 h. The white precipitate obtained was filtered, washed with water and left to dry in an oven at 60 °C. This sample was denoted as SiNC-P. The calcination of SiNC-P was carried out at 500 °C for 5 h and denoted as SiNC-C. The ES-encapsulated silica nanocapsules (SiNC-ES) were prepared by dissolving ES powder in a toluene solution (0.03 M, 0.15 M, 0.3 M and 0.5 M). The preparation procedure was as previously described for the SiNC-P. The sample was denoted as SiNC-ES(*X*), where *X* corresponds to the concentration of sulfur dissolved in 10 mL of toluene.

3. Adsorbent Characterizations

The surface morphology was acquired using field emission scanning electron microscopy (FESEM) model JEOL JSM-6701F. A small portion of adsorbent samples was mounted on the copper stub and putter-coated with a thin layer of gold to avoid electrostatic charging during examination using an accelerating voltage of 0.5-2 kV. The thermogravimetric analysis (TGA) measurement was carried out under nitrogen atmosphere, with a heating rate of 10 °C min^{-1} from 30 °C up to 900 °C using a TGA instrument (Perkin-Elmer model Pyris TGA7, USA). The Fourier transform infra-red (FTIR) spectroscopy was used to identify the functional groups present in the adsorbents. The FTIR spectra were taken from FTIR Spectrometer (PerkinElmer), using a KBr disk pellets method. All the spectra are plotted as transmittances (%) against wavenumber (cm^{-1}) range from 400 cm^{-1} to 4,000 cm^{-1}. The nitrogen adsorption-desorption (NAD) analysis was conducted at a temperature of −196 °C using the Micromeritics apparatus (ASAP 2000). The surface area and porosity characteristics were obtained by the Brunauer-Emmett-Teller (BET) and Barret-Joyner-Halenda (BJH) methods, respectively.

4. Batch Adsorption Experiments

The adsorption performance was carried out in a batch experiment in a 125 mL polycarbonate flask containing 50 mg of adsorbent and 50 mL of Ag(I) solution. The pH of the solution was adjusted using a series of HNO_3 and NaOH solutions. The flask was placed on a rotary shaker and shaken overnight at 200 rpm. After adsorption, the mixture of adsorbent and adsorbate was filtered through 0.45 μm nylon membrane filters, and the filtrate solution was collected for Ag(I) concentration measurement using an inductively coupled plasma optical emission spectroscopy, ICP-OES (Agilent Technologies 700 Series ICP-OES). The adsorption performance was expressed by calculating the adsorption capacity (Q_t) and removal efficiency (η) as described by the following equations:

$$\eta\,(\%)=((C_o-C_e)100)/C_o \quad (1)$$

$$Q_t=(C_o-C_t)V/m \quad (2)$$

where C_o and C_t (mg L^{-1}) are the initial Ag concentration and Ag concentration at time t, respectively. Q_t (mg g^{-1}) is the Ag(I) adsorption capacity at time t, V (L) is the solution volume, and m (g) is the adsorbent mass. Equilibrium adsorption capacity (Q_e) was also calculated using Eq. (2) at C_t=C_e. All adsorption data presented in this study were the result of concentration measurement of triplicate analyses with relative standard deviation of less than 3%.

RESULTS AND DISCUSSION

1. Characterization of SiNC Adsorbents

SiNC adsorbents were prepared via an oil-in-water (o/w) microemulsion single-step polymerization process using TEOS as silica precursor, toluene as co-solvent and NH_4OH as catalyst. In this approach, CTAB surfactant micelles serve as both a structure directing agent and a suitable environment for the entrapment of sulfur molecule in a hydrophobic solvent. When TEOS was added into the o/w microemulsion, the cationic surfactant CTAB that served as micelles self-assembled with the hydrolyzed TEOS through electrostatic interaction and co-condensed on the surface of microemulsion forming CTAB/silica particles [34,47]. The resulting SiNC-P appeared as a white powder, while the SiNC-ES was a yellowish powder with higher sulfur loading; the yellowish color becomes more intense.

The FESEM image of SiNC-P and SiNC-ES shows a cauliflower-like morphology (Fig. 1). The encapsulation of ES promotes modification of morphological structure as can be seen in Fig. 1(b). The cauliflower-like particles of SiNC-ES show clear boundaries among them with almost similar size of smaller grain colonies. The average size of the grains/agglomerated particles was 11 nm.

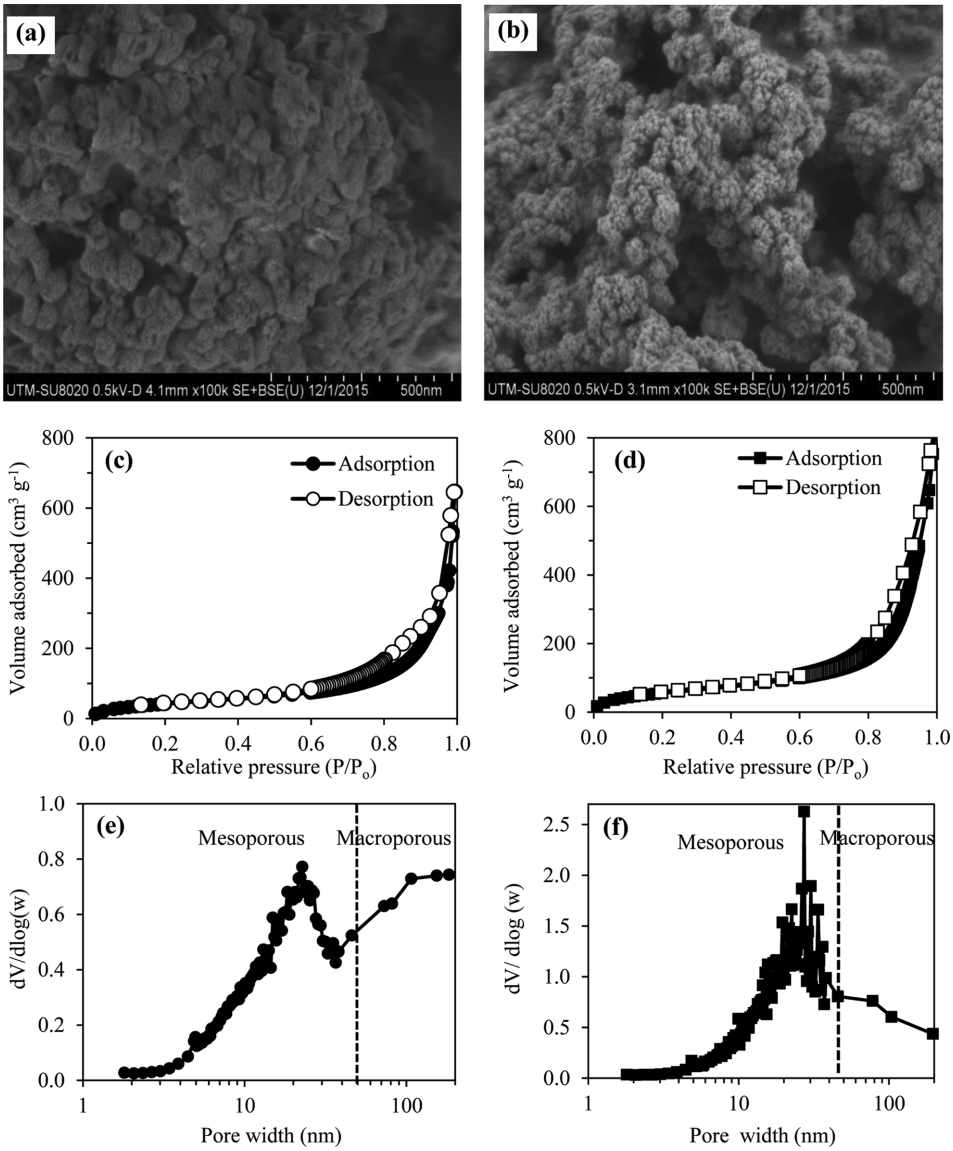

Fig. 1. FESEM images of (a) SiNC-P and (b) SiNC-ES, NAD isotherm of (c) SiNC-P and (d) SiNC-ES, and pore size distribution of (e) SiNC-P and (f) SiNC-ES.

The consistent size of fine agglomerated particles seems to be related to the increase of BET surface area of SiNC-ES (211.33 m^2 g^{-1}) as compared to that of the SiNC-P (157.01 m^2 g^{-1}). The NAD isotherm of SiNC-P (Fig. 1(c)) and SiNC-ES (Fig. 1(d)) shows a typical case for multilayer adsorption in mesoporous materials [48]. The BJH pore size distribution, Figs. 1(e) and 1(f), shows that both samples have a combination of macroporous (D_p>50 nm) and mesoporous (2 nm<D_p<50 nm) size. However, the pore size distribution of silica with the ES encapsulation is decreasing to more mesoporous size, and thus increasing the total pore volume from 0.97 cm^3 g^{-1} for SiNC-P to 1.21 cm^3 g^{-1} for SiNC-ES. This porosity analysis demonstrated that the ES encapsulated silica has mesoporosity and high surface area for the adsorption application. The surface area and pore volume of the ES encapsulated SiNC (SiNC-ES) found in this study were higher than other similar adsorbents reported by Palaniappan et al. [2], although an almost similar synthesis procedure was used. This result indicates that small changes in chemical formulation during the synthesis procedure can significantly affect the properties of the produced adsorbents.

A thermogravimetric experiment was conducted to verify the thermal stability of the materials and to determine the amount of ES encapsulated in the SiNC samples. Fig. 2(a) shows the TG curves of SiNC-P and SiNC-ES(*X*). The TG curve of calcined SiNC-P (denoted as SiNC-C) was added as a reference. The weight loss at temperature below 150 °C was caused by the volatization of water molecules in the SiNC materials. The weight loss (approximately 13%) of SiNC-P was mainly due to the corresponding decomposition of CTAB. The SiNC-ES(0.15) shows an almost similar weight loss profile as SiNC-P. On the derivative weight loss plot, DTG (Fig. 2(b)), two peaks were observed, where the first peak, between 150 °C to 320 °C, was due to CTAB decomposition and an additional peak spotted between 330 °C to 390 °C was related

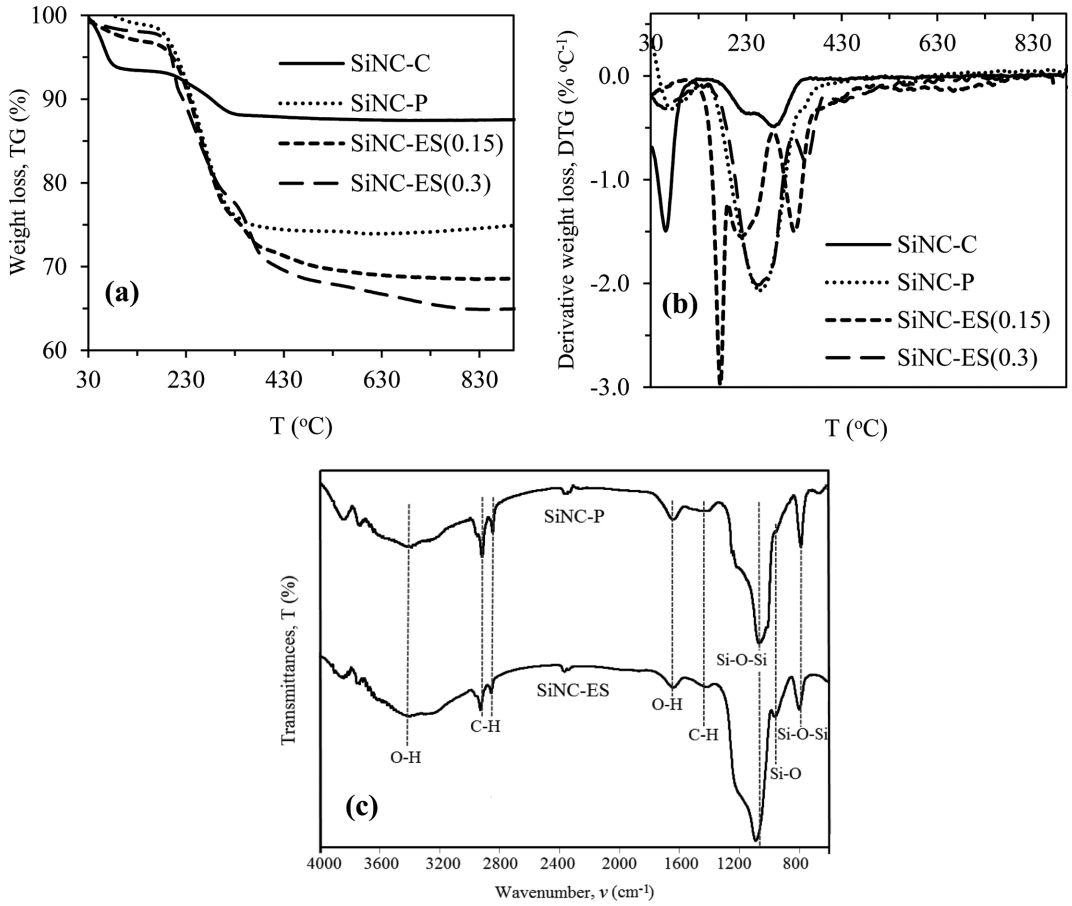

Fig. 2. (a) Thermogravimetric weight loss (TG), (b) derivative thermogravimetric weight loss (DTG), and (c) FTIR spectra of the SiNC adsorbents.

to the sulfur decomposition. The DTG plot of SiNC-ES(0.3), shows three decomposition stages. The first peak at a about 174 °C was the conversion of S_8 rings of ES into a linear polymeric bi-radical molecule (-S-S_6-S-) [49]. The second peaks between 190 °C to 290 °C are related to the CTAB decomposition, and the third weight loss ranging from 290 °C to 390 °C is due to complete sublimation of sulfur. The amount of sulfur estimated from the TG plot of SiNC-ES(0.3) and SiNC-ES(0.15) was 9.5% wt and 6.0% wt, respectively.

The structural information of the prepared adsorbents was analyzed using FTIR. A comparison of FTIR spectra of the SiNC-P and SiNC-ES is shown in Fig. 2(c). The broad peaks at 3,410 cm^{-1} and 1,650 cm^{-1} are attributed to the O-H stretching and O-H bending vibrations of -OH groups from silanol groups and adsorbed water. Two peaks at 2,923 cm^{-1} and 2,849 cm^{-1} correspond to the C-H stretching of CH_2 and CH_3 from the entrapped CTAB. The Si-O-Si symmetric and anti-symmetric stretching vibrations are observed at wavenumber of around 1,060 cm^{-1} and 802 cm^{-1}, respectively. The peaks at 962 cm^{-1} and 460 cm^{-1} correspond to the vibration of Si-OH and Si-O respectively. In general, both SiNC-P and SiNC-ES show similar spectrum patterns, but some of the peaks were shifted to slightly higher values with the addition of sulfur. For example, the peak related to Si-O-Si symmetric vibration and Si-OH shifted to 1,100 cm^{-1} and 975 cm^{-1}, respectively. The peak related to sulfur was not detected in the FTIR spectra.

2. Equilibrium of Ag(I) Adsorption

2-1. Effect on amount of ES Encapsulated Towards Ag(I) Adsorption

The encapsulation of ES in SiNC resulted in a higher adsorption capacity compared to SiNC-P (Fig. 3). The higher the amount

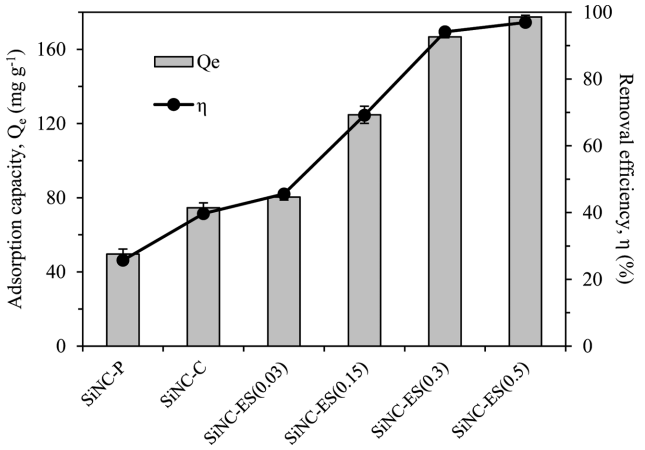

Fig. 3. Effect of sulfur loadings in SiNC adsorbents towards Ag(I) adsorption. Experimental conditions: initial concentration, 30 mg L^{-1}; initial pH, 4; adsorbent loading, 1 g L^{-1}; and contact time, 24 h.

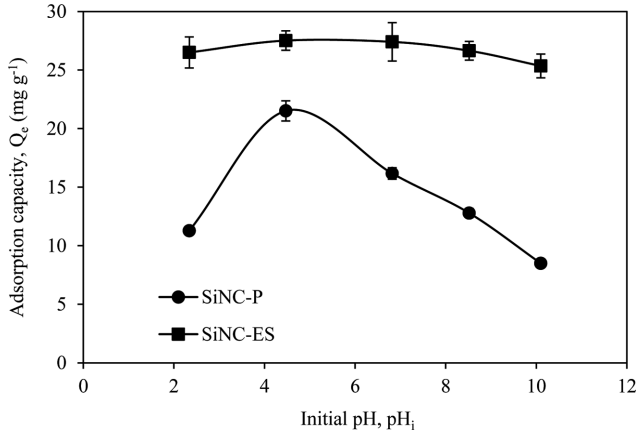

Fig. 4. Effect of initial pH solution towards Ag(I) adsorption. Experimental conditions: adsorbent loading, 1.0 g L^{-1}; initial concentration, 30 mg L^{-1}; contact time, 24 h; and temperature, 30 °C.

of ES encapsulated in the SiNC materials, the higher the Ag(I) adsorption capacity. A small addition of ES can significantly enhance the Ag(I) adsorption. The effect of ES encapsulated in the SiNC towards the Ag(I) adsorption was investigated by varying the molarity of ES dissolved in toluene. The Q_e of SiNC-ES(0.03) enhanced 38.3% as compared to the SiNC-P. The Q_e and removal efficiency of SiNC-ES linearly increased with ES from 0.03 M to 0.3 M. Thereafter, the Q_e and removal efficiency slightly increased with ES concentration. A concentration of ES higher than 0.5 M could not be performed due to the ES solubility problem. According to the TGA analysis, a higher ES loading was obtained by increasing ES concentration used in encapsulation. For instance, the amount of ES encapsulated in SiNC-ES(0.3) was 9.5 wt (%), which was higher than SiNC-ES(0.15) of 6.0 wt (%). Hence, in the proceeding adsorption studies, the SiNC-ES sample was performed using SiNC-ES(0.3).

2-2. Effect of pH Towards Ag(I) Adsorption

The effect of pH values was studied by varying the pH of 30 mg L^{-1} Ag(I) solution ranged from pH 2 to pH 10. The Ag(I) adsorption performance onto SiNC-P and SiNC-ES is shown in Fig. 4. The Ag(I) adsorption capacity onto SiNC-P was highly dependent on pH values. The Q_e was low at pH$_i$ of 2 (11.28 mg g^{-1}), increased to a maximum Q_e (21.51 mg g^{-1}) at pH$_i$ of 4 and thereafter, the Q_e keep decreasing with increasing pH$_i$. On the other hand, less effect of pH$_i$ was observed towards the Ag(I) adsorption onto SiNC-ES.

The variation of Ag(I) adsorption capacity may be related to a factor such as surface charge of adsorbents and speciation of metal ions at various pH values. At very acidic or basic conditions, the presence of H_3O^+ or OH^- ions can increase the competitiveness with positively or negatively charged Ag(I) ions to form an interaction with surface active sites. The acidic or basic conditions also promoted protonation or deprotonation of O-H from silanol groups, increased the repulsion effect with positively or negatively charged Ag(I) ions, hence decreasing the Ag(I) adsorption performance. This electrostatic interaction mechanism is only appropriate to describe the Ag(I) adsorbed onto SiNC-P. The SiNC-ES performed

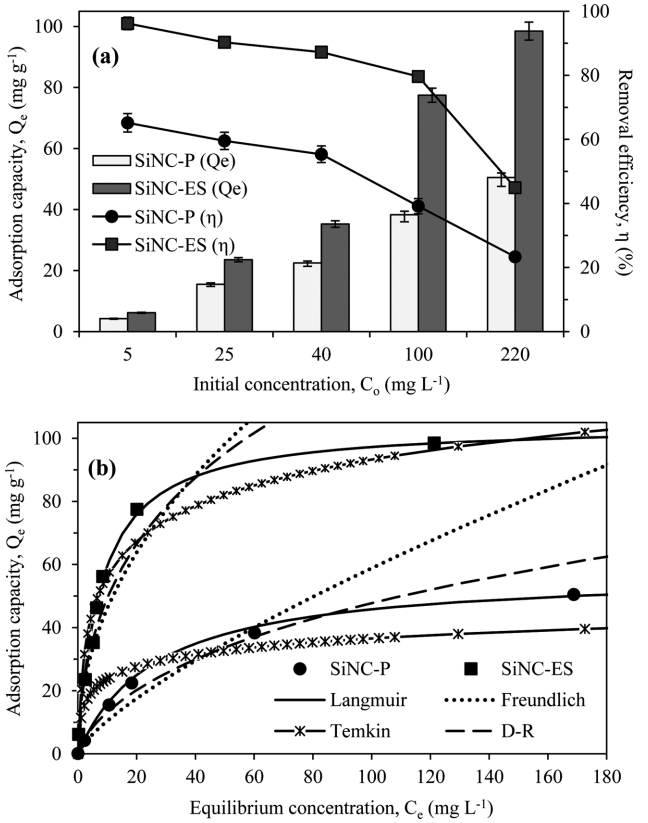

Fig. 5. (a) Effect of initial concentration of Ag solution and (b) Ag(I) adsorption isotherm. Experimental conditions: initial pH, 4, adsorbent loading, 1.0 g L^{-1}; contact time, 24 h; and temperature, 30 °C.

better adsorption as compared to the SiNC-P observed at various pH values. This result is ultimately due to the existence of sulfur functional groups that can form a complexation with Ag(I) ions, therefore increasing the Ag(I) adsorption performance of the adsorbent materials.

2-3. Effect of Concentration and Adsorption Isotherm

The experiments on the effect of concentration towards Ag(I) adsorption onto synthesized SiNC adsorbents were carried out by varying the initial Ag(I) concentration, C_o from 5 mg L^{-1} to 220 mg L^{-1}. The results in Fig. 5(a) show that the SiNC-ES exhibited a strong adsorption affinity towards Ag(I). The Q_e of Ag(I) increased while the Ag(I) removal efficiency, η decreased with the increasing C_o. For a fixed adsorbent dosage, the total available sites are limited for Ag(I) in the solution to be adsorbed at higher concentration, thus leading to a decrease of the η. The increase of concentration also could increase the mass transfer due to the increasing driving force to counter all mass transfer resistance between aqueous and solid phase, therefore increasing the Q_e.

The Ag(I) adsorption isotherm is shown in Fig. 5(b). The maximum adsorption capacity ($Q_{e,max}$) of SiNC-ES was 98.51 mg g^{-1}, which is higher than SiNC-P (50.49 mg g^{-1}). Table 1 shows the comparison of maximum Ag(I) adsorption capacity, $Q_{e,max}$ of SiNC adsorbents with other adsorbents reported by the previous researchers. The modified polymeric materials showed higher adsorption capacity compared to other adsorbents. Comparing the $Q_{e,max}$ of

Table 1. Ag(I) adsorption capacity for various adsorbents

Adsorbents	Active groups	$Q_{e.max}$ (mg g^{-1})	References
Silica materials			
SiNC-P	-	50.5	This study
SiNC-ES	Elemental sulfur	98.5	
MPTMS-silica bead (SSB)	Thiol	75.8	Quang et al. [23]
ATT-SNP	Amino, thiol, triazol	124.5	Fu et al. [25]
Carbon/char			
Chitosan/bamboo charcoal	-	52.9	Nitayaphat and Jintakosol [4]
Magnetic carbon	-	56.0	Condomitti et al. [5]
Activated carbon (almond shell)	-	59.5	Omri and Benzina [6]
$Ni_{0.5}Zn_{0.5}Fe_2O_4$/ASA[2]	$Ni_{0.5}Zn_{0.5}Fe_2O_4$	243.9	Beigzadeh and Moeinpour [7]
Polymers/resins			
Dedoped Fe_3O_4/PPy	Amino	143.3	Peng et al. [12]
Penta3MP4/PEG-DA/HEMA	Thiol-ene	102.0	Fırlak [13]
Ambersep™ GT74	Thiol	328.0	Nawaz and Sengupta [11]
PSGA resin	Amidoxime-guanidine	212.0	Wang et al. [10]
Polystyrene-trimercaptotriazine	Thiol	187.1	Wang et al. [9]
Thioureas-modified chitosan	Thiourea	403.3	Wang et al. [8]
Biomaterials			
Coffee ground/PVA beads	-	35.0	Jeon [16]
Coconut fiber, CF (Pure)	-	54.1	Saman et al. [17]
CF-NaOH	-	66.0	
Coconut pith, CP-Pure	-	53.9	Saman et al. [18]
CP-NaOH	-	51.8	
CP-BTESPT	Tetrasulfide	66.9	
Clays/zeolites/soils			
Verdelodo bentonite[1]	-	100.3	Freitas et al. [3]
Holloysite nanotubes		109.8	Kiani [19]
Raw vermiculite	-	46.2	Sarı and Tüzen [20]
MnO-vermiculite	MnO	69.2	Sarı and Tüzen [20]
Clinoptilolites (*Çankırı-Çorum*)	-	31.4	Çoruh et al. [21]
Clinoptilolites (*Manisa-Gördes*)	-	22.6	Çoruh et al. [21]
Metal oxides			
MBI-Nano-TiO_2	Mercapto	128.2	Pourreza et al. [22]

SiNCs with other silica materials, the ATT-SNP has higher $Q_{e.max}$ than the SiNC-ES, but the synthesis of ATT-SNP is relatively complicated as compared to the SiNC-ES.

The adsorption isotherm data were analyzed using common isotherm models, namely the Langmuir, Freundlich, Dubinin-Raduskevich (D-R) and Temkin models. The mathematical relationship and calculated constant parameters of each model are shown in Table 2. The isotherm constants were determined from the isotherm linear plot. The Langmuir model assumes monolayer adsorption capacity (Q_L) is equivalent to the number of active sites present in the adsorbents. The Q_L values are slightly higher than the experimental values. The essential feature of the Langmuir model, which is the dimensionless separation factor, R_L indicates that the adsorption is favorable. The magnitude of n from the Freundlich models was in the range of 1 to 10, also indicating a favorable adsorption system. The D-R and Temkin isotherms are temperature-dependent models that provide additional information about the binding energy of the adsorbate-adsorbent interaction. The mean free energies from the D-R isotherm (E_{D-R}) of Ag(I) adsorption onto SiNC-P and SiNC-ES were 9.618 kJ mol^{-1} and 11.493 kJ mol^{-1}, respectively. The values fall in the region of ion-exchange interaction (8 kJ mol^{-1}<E_a<16 kJ mol^{-1}) [50]. An analysis of the Temkin model shows that the constant related to the binding energy (b_T) indicates the adsorption was governed by chemisorption interaction. The calculated constants then were used to plot the predicted isotherm curves (Fig. 5(b)). By considering the regression coefficient value (R^2) and isotherm fitting (Fig. 5(b)) of each isotherm model, the Langmuir model was chosen as the best model to describe the adsorption isotherm of Ag(I) adsorption onto both SiNC-P and SiNC-ES. Previous studies also found that the Langmuir model to be the best fitted model to describe the isotherm data of Ag(I) onto various adsorbents such

Table 2. Adsorption isotherm parameters of Ag(I) adsorption

Isotherm models	Parameters	SiNC-P	SiNC-ES
Experimental values	$Q_{e.max}$ (mg g^{-1})	50.49	98.51
Langmuir: $C_e/Q_e=(1/Q_Lb)+(C_e/Q_L)$			
	Q_L (mg g^{-1})	57.844	104.594
	b (L mg^{-1})	0.038	0.132
	R_L for C_o of (5-220) mg L^{-1}	$0.840<R_L<0.107$	$0.602<R_L<0.033$
	R^2	0.9943	0.9980
Freundlich: $\ln Q_e=\ln k_f+1/n \ln C_e$			
	k_f ($L^n mg^{1-n}$ g^{-1})	1.844	15.641
	n	1.330	2.130
	R^2	0.9762	0.9211
Dubinin-Radushkevich (D-R): $\ln Q_e=\ln Q_{D\text{-}R}-2\beta_{D\text{-}R}\varepsilon^2$			
where $\varepsilon=RT \ln(1-1/C_e)$			
	$Q_{D\text{-}R}$ (mg g^{-1})	254.898	392.708
	$-\beta_{D\text{-}R}\times10^9$ (mol J^{-1})	5.405	3.786
	E (kJ mol^{-1})	9.618	11.493
	R^2	0.9968	0.9656
Temkin: $Q_e=(RT/b_T)\ln A_T+(RT/b_T)\ln C_e$			
	b_T (kJ mol^{-1})$\times10^{-4}$	4.899	1.692
	A_T (L $mmol^{-1}$)	782.467	357.655
	R^2	0.7668	0.9275

$Q_{e.max}$ is maximum adsorption capacity from isotherm plot; Q_L is monolayer adsorption capacity; b_L is Langmuir constant related to adsorption affinity; k_f related to adsorption capacity; n Freundlich constant. $Q_{D\text{-}R}$ adsorption capacity calculated from D-R model; $\beta_{D\text{-}R}$ is D-R constant; $E_{D\text{-}R}$ is activation energy from D-R; A_T is Temkin isotherm constant; and β_T is heat of adsorption energy.

as MPTMS-silica bead [23], ATT-SNP [25], trithiocryanuric acid modified poly(glycidyl methacrylate) microspheres [14], penta3MP4/PEG-DA/HEMA [13], Fe_3O_4@polydopamine core-shell microspheres [15], and PSGA resin [10].

3. Adsorption Kinetics and Mechanisms

The adsorption behavior of Ag(I) as a function of contact time is shown in Fig. 6. For the first 20 min of contact time, the adsorption rate was rapid, then it proceeded at a slower rate until it achieved equilibrium. The rapid initial adsorption rate was due to large availability of active sites at the initial stage that increased the concentration gradient between adsorbate in solution and adsorbate at the adsorbent surface. The SiNC-ES shows a higher adsorption rate as compared to SiNC-P. This could be expected because SiNC-ES has a high surface area and additional sulfur active groups that are attracted towards Ag(I) ions.

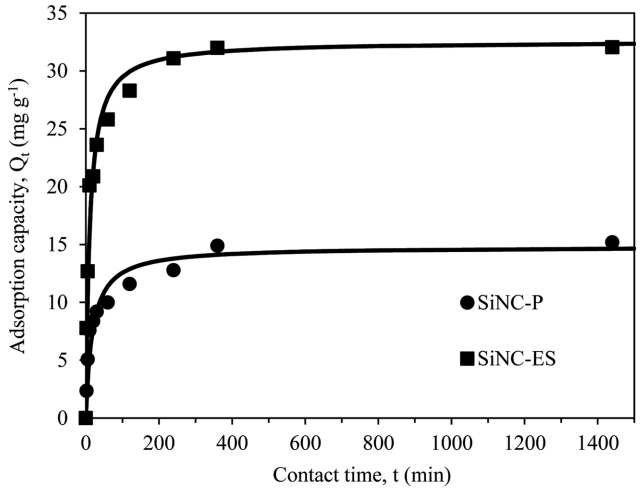

Fig. 6. Effect of contact time on the Ag(I) adsorption onto SiNC adsorbents. Experimental conditions: adsorbent loading, 1.0 g L^{-1}; initial concentration, 28 mg L^{-1}; initial pH, 4; and temperature, 30 °C.

A typical adsorption process first involves the transfer process of Ag(I) ions to the adsorbent surface through three stages of diffusion steps: (i) migration of Ag(I) ions from bulk solution to the adsorbent surface (bulk diffusion); (ii) migration pass through the boundary layer of adsorbent (film diffusion); and (iii) migration at adsorbent pores and surfaces (intra-particle diffusion). This is subsequently followed by chemical interactions between Ag(I) ions with active sites. These adsorption steps are well described and various models have been developed to analyze the steps [51-54].

The diffusion steps are easily interpreted using the Weber-Morris plot (Fig. 7(a)). The plot shows three linear portions which indicate three diffusion stages of the adsorption process. The first, second and third stages represent film diffusion, intra-particle diffusion and final equilibrium stage, respectively. The rate constant (k_d) values obtained from the Weber-Morris plot for each adsorption stage are given in Table 3. It was found that the $k_{d1}>k_{d2}>k_{d3}$ indicating the first stage was faster compared to other two stages. The faster rate at the beginning of adsorption is due to the vast transfer of

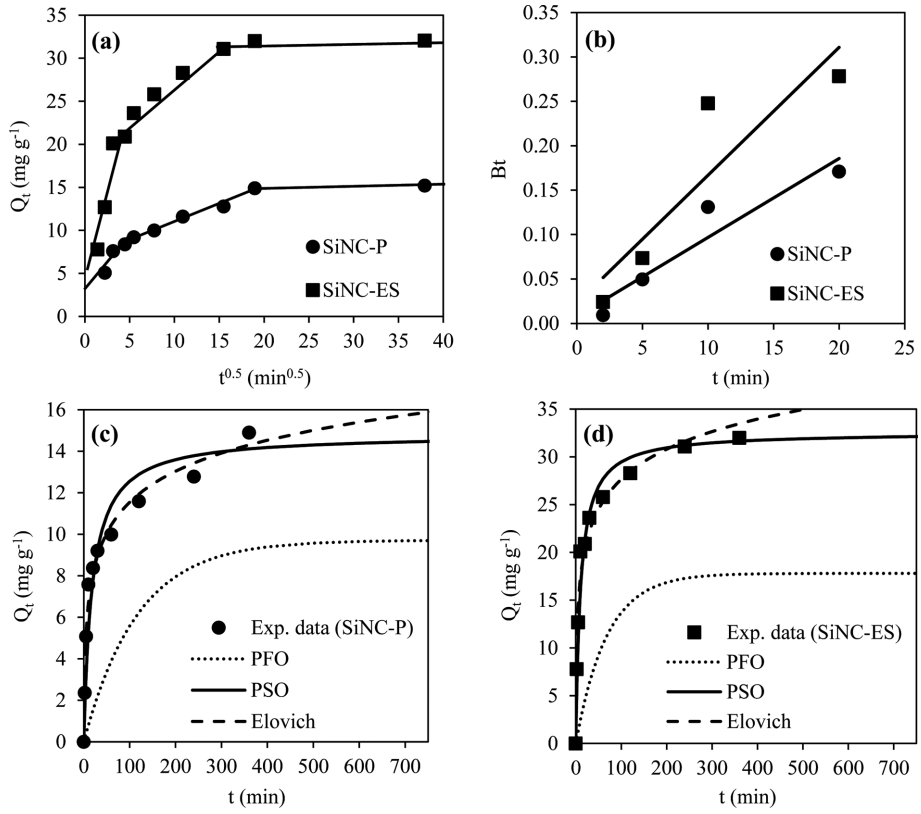

Fig. 7. Kinetic models plots of Ag(I) adsorption onto SiNC adsorbents: (a) Weber-Morris plot; (b) Boyd plot; and (c), (d) comparison of chemical reaction kinetic model fitting.

adsorbate at the external adsorbent surfaces. As time progresses, the external surfaces become saturated and the adsorbate then will diffuse into the adsorbate pores until it reached saturation [55].

The overall mass transfer stage is controlled by either film of intra-particle diffusion, because the bulk diffusion step was neglected since the adsorption experiment was performed at rapid stirring. The Weber-Morris plot clearly shows the first line did not pass through the origin, thereby film diffusion and intra-particle diffusion could be the controlling steps [56]. To determine the controlling step between these two steps, the Boyd kinetic expression was employed [54,57,58]. The Boyd plot of Bt versus time of the initial Ag(I) adsorption period is shown in Fig. 7(b). Bt can be expressed by the following equations [55]:

$$Bt = -0.4977 - \ln(1-F), \quad F \text{ value} > 0.85 \tag{3}$$

$$Bt = (\sqrt{\pi} - \sqrt{[\pi - (\pi^2 F/3)]})^2, \quad F \text{ value} < 0.85 \tag{4}$$

where F is equal to Q_t/Q_e. The plot shows a straight line and crosses the Y-axis, which indicates that film diffusion is the rate controlling step. The quantitative analysis was further demonstrated by comparing the film (D_f) and intra-particle (D_{eff}) diffusion coefficient values. The D_f was calculated from the slope of Q_t/Q_e versus $t^{0.5}$, according to the following equation:

$$(Q_t/Q_e) = 6(D_f/\pi R_P^2))^{0.5} t^{0.5} \tag{5}$$

R_P is the radius of adsorbent particles (cm). The value of D_f found for Ag(I) adsorption onto SiNC-P and SiNC-ES was 4.59×10^{-12} cm^2/min and 5.32×10^{-12} cm^2/min, respectively. The intra-particle diffusion coefficient (D_{eff}) was calculated according to Eq. (6) using the slope (s) of the Boyd plot.

$$s = \pi^2 D_{eff}/R_p^2 \tag{6}$$

The D_{eff} values of Ag(I) adsorption onto SiNC-P and SiNC-ES were 4.75×10^{-10} cm^2/min and 7.69×10^{-10} cm^2/min, respectively. The value of D_f was smaller than D_{eff}; thus, film diffusion is slower than intra-particle diffusion, confirming film diffusion as the rate-limiting step.

The kinetic data also were analyzed using the chemical reaction-kinetic based model: namely, the pseudo-first order (PFO), pseudo-second order (PSO), and Elovich model. The kinetic model equations and calculated model constants are tabulated in Table 3. The results suggest that the Ag(I) adsorption by SiNCs can be well described by the PSO kinetic model. This conclusion is based on the fact that the R^2 values of the PSO were the highest and the non-linear fitting (Fig. 7(c) and 7(d)) was also closer to the experimental data compared to the PFO and Elovich models. The PSO also fitted well to the kinetic data of Ag(I) adsorption onto ATT-SNP [25], trithiocryanuric acid modified poly(glycidyl methacrylate) microspheres [14], Fe_3O_4@polydopamine core-shell microspheres [15], and PSGA resin [10]. The predicted adsorption capacity from the PSO (Q_{e2}) of both Ag(I) adsorption onto SiNC-P and SiNC-ES is close to the experimental Q_e. The chemical interaction at SiNC adsorbents surfaces was attributed to the presence of oxygen from siloxane structure of silicas, nitrogen from CTAB and sulfur from ES encapsulation. These groups can interact chemically with Ag(I)

Table 3. Kinetic modeling parameters of Ag(I) adsorption

Kinetic models	Parameters	SiNC-P	SiNC-ES
Experimental values			
Q_e (mg g^{-1})		15.20	32.05
Initial adsorption rate (mg min^{-1})		0.305	0.501
Mass transfer process			
Weber-Morris: $Q_t=k_{dn}t^{0.5}$			
	k_{d1} (mg $min^{-0.5}$)	1.959	4.447
	R^2	0.8955	0.8687
	k_{d2} (mg $min^{-0.5}$)	0.420	0.904
	R^2	0.9739	0.9582
	$k_{d3}\times10^2$ (mg $min^{-0.5}$)	1.569	0.319
	R^2	0.9999	0.9999
Chemical interaction models			
Pseudo-first order (PFO): $\ln(Q_e-Q_t)=\ln Q_{e1}-k_1t$			
	Q_{e1} (mg g^{-1})	9.710	17.802
	$k_1\times10^2$ (min^{-1})	0.855	1.467
	h_{o1} (mg g^{-1} min^{-1})	0.083	0.261
	R^2	0.9187	0.9671
Pseudo-second order (PFO): $t/Q_t=(1/k_2Q_{e2}^2)+(t/Q_{e2})$			
	Q_{e2} (mg g^{-1})	14.819	32.575
	$k_2\times10^3$ (mg min^{-1})	3.745	2.909
	h_{o2} (mg g^{-1} min^{-1})	0.823	3.087
	R^2	0.9893	0.9989
Elovich: $Q_t=\beta\ln(\propto\beta)+\ln t$			
	β (g mg^{-1})	0.463	0.220
	α (mg g^{-1} min^{-1})	4.506	19.906
	R^2	0.9762	0.9627

K_{dn} is the adsorption rate calculated from the Weber-Morris plot, Q_{e1} and Q_{e2} is adsorption capacity calculated from PFO and PSO kinetic models, respectively. k_1 and k_2 is adsorption rate constant from PFO and PSO kinetic models, respectively. h_{o1} and h_{o2} is initial adsorption rate constant from PFO and PSO kinetic models, respectively. β is Elovich model constant depicts the extent of surface coverage, while α is a constant related to chemisorption rate.

ions in various ways which can be weak chemical interaction (physisorption due to attraction forces) and/or strong chemical interaction (e.g. complexation).

4. Recyclability Studies

Besides high efficiency and selectivity, recyclability of the adsorbent is an important factor to be considered for the practical application of adsorbent in the precious metals recovery [42]. In this work, the recyclability of SiNC-ES was evaluated through several adsorption-desorption cycle experiments. The Ag(I) adsorption experiments were performed under the respective batch experimental conditions with 30 mg L^{-1} of initial Ag(I) concentration. After adsorption, the Ag-loaded adsorbent was collected and the batch desorption experiments were conducted using 1% acidic thiourea solution (in 1 M HCl) as eluting agent and agitated at 200 rpm for 12 h.

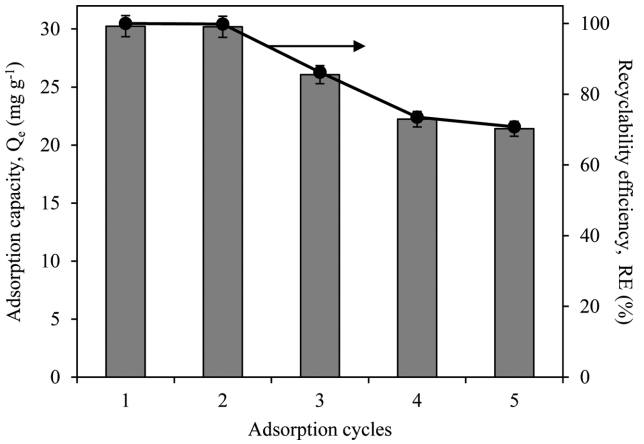

Fig. 8. Adsorption performance of recyclable SiNC-ES.

The Ag(I) removal efficiency for recyclable SiNC-ES is shown in Fig. 8. The Ag(I) adsorption capacity of the first two cycles of reused adsorbent was maintained around 30.20 mg g^{-1}. The Q_e dropped to 26.07 mg g^{-1} and 22.23 mg g^{-1} in the third and fourth adsorption cycles, respectively. After that, the adsorption capacity slightly dropped to about 21.40 mg g^{-1}. During the desorption experiment, the pre-adsorbed Ag(I) ions were not totally eluted; therefore, less active sites were available for further adsorption experiment cycles, thus reducing the adsorption performance of the regenerated SiNC-ES. However, the recyclability efficiency (RE) for all regenerated adsorbent was all above 70%, suggesting good recyclability of the SiNC-ES. The recyclability efficiency is defined as the percentage adsorption capacity of n-cycle of regenerated adsorbent to the fresh adsorbent.

5. Selectivity of SiNC-ES Towards Ag(I) in Industrial Waste Solution

From the equilibrium adsorption of SiNC-ES towards Ag(I) using a synthetic test solution, a highly encouraging result was obtained. Thus, the applicability of adsorbent to adsorb Ag(I) in a real industrial waste was conducted. In this study, a photographic waste solution (PWS) was used as a medium and the adsorption was conducted under the same procedure described earlier. The concentration of Ag(I) ions in the PWS was relatively low; therefore, 3.0 mmol L^{-1} of Ag(I) solution was spiked into the PWS medium. The initial pH of PWS was 1.85 and increased to 4.01 by the addition of Ag(I) solution.

The PWS consists of many anions and cations that could significantly affect the adsorption performance towards the specific metal ions. Table 4 shows the adsorption performance of selected cations in PWS using SiNC-ES adsorbent. Initial concentrations of Fe, K and N were relatively higher compared to the Ag and Pb, while Zn existed at very low concentration. The Q_e of cations increased in the following order: Zn>Ag>Pb>Fe>K>Na, a similar order with the increasing C_o except for K and Na. The Ag(I) removal efficiency, however, was the highest among other cations, although the C_o of Ag(I) was relatively low compared to the other cations. The quantitative selectivity analysis of Ag(I) adsorption was evaluated by the distribution coefficient value (K_{dc}) and was calculated using Eq. (7).

Table 4. Adsorption performance of selected cations in PWS using SiNC-ES

Cations	C_o (mmol L^{-1})	η (%)	Q_e (mmol g^{-1})	K_{dc} (L g^{-1})
Ag	0.30±0.00	90.46±0.44	0.26±0.00	0.88±0.00
Zn	0.02±0.00	56.47±6.10	0.01±0.00	0.55±0.06
Pb	0.49±0.00	68.38±2.01	0.33±0.01	0.67±0.02
Fe	17.18±0.03	3.78±0.20	0.64±0.03	0.04±0.00
Na	39.97±0.11	2.10±0.12	0.82±0.05	0.02±0.00
K	61.64±0.09	1.26±0.20	0.76±0.12	0.01±0.00

$$K_{dc}=((C_o-C_e)/C_e)\times(V/m) \quad (7)$$

The higher K_{dc} value suggests a higher selectivity of adsorbent towards metal ions; thus, the SiNC-ES has a high selectivity towards Ag(I), followed with Pb and Zn. High selectivity of sulfur-containing adsorbent towards Ag(I) was expected, in conformity with the hard and soft acids and bases (HSAB) theory, where hard acids prefer to interact with hard bases and soft acids prefer soft bases [59]. Besides sulfur functional groups, the SiNC-ES is also loaded with oxygen from silanol groups that provided additional active sites for chemical interactions with other cations like Pb, Zn and Fe. However, the removal efficiency and Q_e of Fe was too low compared to Zn and Pb, although all three ions are classified under the same category (intermediate region between hard and soft acids). This result is due to extremely higher concentration of Fe ions in the PWS compared to the concentration of Pb and Zn ions.

CONCLUSIONS

Elemental sulfur (ES) encapsulated silica nanocapsules (SiNC-ES) were successfully prepared using a facile synthesis method of the one-step water in oil microemulsion polymerization process which was confirmed by FTIR and TGA analyses. The encapsulation of ES increased the surface area and porosity of the SiNC-P. The SiNC-ES shows a better Ag(I) adsorption performance having a maximum adsorption capacity of 98.51 mg g^{-1} than SiNC-P (50.49 mg g^{-1}), adsorption increased with ES loading and pH independence, and the isotherm data follow the Langmuir model. The kinetics of Ag(I) adsorption onto SiNC-ES obeyed the pseudo-second-order (PSO) model having film diffusion as the controlling step. The SiNC-ES shows high selectivity and can be regenerated. Thus, it offers a great potential as an adsorbent for Ag(I) recovery from industrial wastewater such as a photographic waste solution.

ACKNOWLEDGEMENTS

The financial support from the Universiti Teknologi Malaysia (UTM) for the Research University Grant (GUP 15H77) and UTM Postdoctoral Fellowship Scheme (PDRU 04E72 and PDRU 03E92) awarded to Norasikin Saman and Safia Syazana Mohtar are gratefully acknowledged.

CONFLICT OF INTEREST

The authors declare that they have no conflict of interest.

REFERENCES

1. X. Lu, Q. Yin, Z. Xin and Z. Zhang, *Chem. Eng. Sci.*, **65**, 6471 (2010).
2. T. Palaniappan, N. Saman, H. Mat and K. Johari, *AIP Conf. Proceed.*, **1901**, 020018 (2017).
3. E. D. Freitas, A. C. R. Carmo, A. F. Almeida Neto and M. G. A. Vieira, *Appl. Clay Sci.*, **137**, 69 (2017).
4. W. Nitayaphat and T. Jintakosol, *J. Cleaner Prod.*, **87**, 850 (2015).
5. U. Condomitti, A. T. Silveira, G. W. Condomitti, S. H. Toma, K. Araki and H. E. Toma, *Hydrometallurgy*, **147-148**, 241 (2014).
6. A. Omri and M. Benzina, *Desalin. Water Treat.*, **51**, 2317 (2013).
7. P. Beigzadeh and F. Moeinpour, *Trans. Nonferrous Met. Soc. China*, **26**, 2238 (2016).
8. L. Wang, R. Xing, S. Liu, H. Yu, Y. Qin, K. Li, J. Feng, R. Li and P. Li, *J. Hazard. Mater.*, **180**, 577 (2010).
9. S. Wang, H. Li, X. Chen, M. Yang and Y. Qi, *J. Environ. Sci.*, **24**, 2166 (2012).
10. Y. Wang, X. Ma, Y. Li, X. Li, L. Yang, L. Ji and Y. He, *Chem. Eng. J.*, **209**, 394 (2012).
11. T. Nawaz and S. Sengupta, *Sep. Purif. Technol.*, **176**, 145 (2017).
12. X. Peng, W. Zhang, L. Gai, H. Jiang, Y. Wang and L. Zhao, *Chem. Eng. J.*, **280**, 197 (2015).
13. M. Fırlak, M. V. Kahraman, E. K. Yetimoğlu and B. Zeytuncu, *Sep. Sci. Technol.*, **48**, 2860 (2013).
14. C. Xiong, S. Wang, L. Zhang, Y. Li, Y. Zhou and J. Peng, *J. Mol. Liq.*, **254**, 340 (2018).
15. M. Wu, Y. Li, R. Yue, X. Zhang and Y. Huang, *Sci. Sep.*, **7**, 42773 (2017).
16. C. Jeon, *J. Ind. Eng. Chem.*, **53**, 261 (2017).
17. N. Saman, K. Johari, S. T. Song and H. Mat, *Sep. Sci. Technol.*, **50**, 937 (2015).
18. N. Saman, K. Johari, S. S. Tien and H. Mat, *J. Natural Fibers*, **12**, 283 (2015).
19. G. Kiani, *Appl. Clay Sci.*, **90**, 159 (2014).
20. A. Sarı and M. Tüzen, *Micropor. Mesopor. Mater.*, **170**, 155 (2013).
21. S. Çoruh, G. Şenel and O. N. Ergun, *J. Hazard. Mater.*, **180**, 486 (2010).
22. N. Pourreza, S. Rastegarzadeh and A. Larki, *J. Ind. Eng. Chem.*, **20**, 127 (2014).
23. D. V. Quang, J. E. Lee, J.-K. Kim, Y. N. Kim, G. N. Shao and H. T. Kim, *Powder Technol.*, **235**, 221 (2013).
24. I. H. Arellano, S. H. Madani, J. Huang and P. Pendleton, *Chem. Eng. J.*, **283**, 692 (2016).
25. L. Fu, L. Zhang, S. Wang, J. Peng and G. Zhang, *J. Mol. Liq.*, **241**, 292 (2017).
26. A. F. Moreira, D. R. Dias and I. J. Correia, *Micropor. Mesopor. Mater.*, **236**, 141 (2016).
27. A. F. Moreira, C. F. Rodrigues, C. A. Reis, E. C. Costa and I. J. Correia, *Micropor. Mesopor. Mater.*, **270**, 168 (2018).
28. M. J. Barnabas, S. Parambadath and C.-S. Ha, *J. Ind. Eng. Chem.*, **53**, 392 (2017).
29. Y. Zhou, G. Quan, Q. Wu, X. Zhang, B. Niu, B. Wu, Y. Huang, X. Pan and C. Wu, *Acta Pharm. Sin. B*, **8**, 165 (2018).
30. X. Wang, H. Chen, Y. Zheng, M. Ma, Y. Chen, K. Zhang, D. Zeng and J. Shi, *Biomaterials*, **34**, 2057 (2013).
31. H. Miyoshi, F. Kida, H. Hase and K. Tsuchiya, *Phys. Procedia*, **80**,

90 (2015).
32. L. S. Chin, M. Lim, T. T. Hung, C. P. Marquis and R. Amal, *RSC Adv.*, **4**, 13052 (2014).
33. J. Fang, Y. Zhang, Y. Zhou, S. Zhao, C. Zhang, H. Zhang, X. Sheng and K. Wang, *Langmuir*, **33**, 2698 (2017).
34. L. Wu, H. Zhang, M. Wu, Y. Zhong, X. Liu and Z. Jiao, *Micropor. Mesopor. Mater.*, **228**, 318 (2016).
35. R. Lv, J. Peng, S. Chen, Y. Hu, M. Wang, J. Lin, X. Zhou and X. Zheng, *Sens. Actuators B Chem.*, **250**, 721 (2017).
36. L. Ruggiero, L. Crociani, E. Zendri, N. El Habra and P. Guerriero, *Appl. Surf. Sci.*, **439**, 705 (2018).
37. F. Maia, A. P. Silva, S. Fernandes, A. Cunha, A. Almeida, J. Tedim, M. L. Zheludkevich and M. G. S. Ferreira, *Chem. Eng. J.*, **270**, 150 (2015).
38. F. Maia, J. Tedim, A. C. Bastos, M. G. S. Ferreira and M. L. Zheludkevich, *Nanotechnology*, **24**, 415502 (2013).
39. L. Liu, G. Alva, X. Huang and G. Fang, *Renew. Sust. Energy Rev.*, **66**, 399 (2016).
40. Z. Mao, Q. Wu, M. Wang, Y. Yang, J. Long and X. Chen, *Nanoscale Res Lett.*, **9**, 501 (2014).
41. L. I. Abd Ali, W. A. Wan Ibrahim, A. Sulaiman, M. A. Kamboh and M. M. Sanagi, *Talanta*, **148**, 191 (2016).
42. N. F. Abd Razak, M. Shamsuddin and S. L. Lee, *Chem. Eng. Res. Design*, **130**, 18 (2018).
43. Y. Li, Y. Wei, S. Huang, X. Liu, Z. Jin, M. Zhang, J. Qu and Y. Jin, *J. Mol. Liq.*, **269**, 824 (2018).
44. K. Johari, N. Saman and H. Mat, *J. Mater. Eng. Perform.*, **23**, 809 (2014).
45. N. Saman, K. Johari and H. Mat, *Micropor. Mesopor. Mater.*, **194**, 38 (2014).
46. N. Saman, K. Johari, H. Kong, S. S. Mohtar, O. Hassan, N. Ali and H. Mat, *Chem. Eng. Res. Design*, **144**, 198 (2019).
47. E. Che, L. Wan, Y. Zhang, Q. Zhao, X. Han, J. Li, J. Liu and S. Wang, *Asian J. Pharm. Sci.*, **9**, 317 (2014).
48. S. J. Gregg and K. S. W. Sing, *Adsorption, surface area and porosity*, 2nd Ed., Academic Press, London (1995).
49. G. Carotenuto, V. Romeo, S. D. Nicola and L. Nicolais, *Nonoscale Res. Lett.*, **8**, 94 (2013).
50. C.-S. Zhu, L.-P. Wang and W.-B. Chen, *J. Hazard. Mater.*, **168**, 739 (2009).
51. Y. S. Ho, J. C. Y. Ng and G. McKay, *Sep. Purif. Methods*, **29**, 189 (2000).
52. M. A. Fulazzaky, Z. Majidnia and A. Idris, *Chem. Eng. J.*, **308**, 700 (2017).
53. M. A. Wahab, S. Jellali and N. Jedidi, *Bioresour. Technol.*, **101**, 8606 (2010).
54. N. Saman, K. Johari, S.-T. Song, H. Kong, S.-C. Cheu and H. Mat, *J. Environ. Chem. Eng.*, **4**, 2487 (2016).
55. B. H. Hameed and M. I. El-Khaiary, *J. Hazard. Mater.*, **154**, 237 (2008).
56. F. Pagnanelli, S. Mainelli, F. Vegliò and L. Toro, *Chem. Eng. Sci.*, **58**, 4709 (2003).
57. S. Banerjee and M. C. Chattopadhyaya, *Arabian J. Chem.*, **10**, S1629 (2017).
58. N. Saman, K. Johari, S.-T. Song, H. Kong, S.-C. Cheu and H. Mat, *Chemosphere*, **171**, 19 (2017).
59. R. G. Pearson, *J. Chem. Educ.*, **45**, 581 (1968).